A solvent-free and vacuum-free melt-processing method to fabricate highly crystalline organic semiconducting layers for organic electronic applications

Journal:	*Journal of Materials Chemistry C*
Manuscript ID	TC-ART-09-2018-004834.R1
Article Type:	Paper
Date Submitted by the Author:	18-Dec-2018
Complete List of Authors:	Ribierre, Jean-Charles; Kyushu University, Center for Organic Photonics and Electronics Research Li, Zhao; Kyushu University, Center for Organic Photonics and Electronics Research (OPERA) Liu, Xiao ; Sorbonne Universités Lacaze, Emmanuelle; Institut des Nanosciences de Paris, CNRS Heinrich, Benoît; IPCMS Strasbourg, Département des Matériaux Organiques Méry, Stéphane; IPCM Strasbourg, DMO Sleczkowski, Piotr; Ewha Womans University, Physics Xiao, Yiming ; Ewha Womans University Lafolet, Frédéric; Université Joseph Fourier, Département de Chimie Moléculaire (CNRS, UMR-5250) hashizume, Daisuke; Riken, Aoyama, Tetsuya; RIKEN, Uchiyama, Masanobu; Rikagaku Kenkyujo, Wu, Jeong Weon; Ewha Womans University, Department of Physics, CNRS Ewha International Research Center Zaborova, Elena; Aix Marseille Universite, CINaM UMR 7325 Fages, Frederic; Aix Marseille Universite, CINaM UMR 7325 Daleo, Anthony ; Aix Marseille Universite, CINaM UMR 7325 Mathevet, Fabrice; Université Pierre et Marie Curie, Institut Parisien de Chimie Moleculaire Adachi, Chihaya; Kyushu University, Center for Organic Photonics and Electronics Research (OPERA)

Journal Name

ARTICLE

A solvent-free and vacuum-free melt-processing method to fabricate organic semiconducting layers with large crystal size for organic electronic applications

Received 00th January 20xx,
Accepted 00th January 20xx

DOI: 10.1039/x0xx00000x

www.rsc.org/

Jean-Charles Ribierre [ab]*, Li Zhao,[a] Xiao Liu,[cd] Emmanuelle Lacaze,[d] Benoît Heinrich,[e] Stephane Méry,[e] Piotr Sleczkowski,[f] Yiming Xiao,[f] Frédéric Lafolet,[gh] Daisuke Hashizume,[i] Tetsuya Aoyama,[j] Masanobu Uchiyama,[jk] Jeong Weon Wu,[fl] Elena Zaborova,[m] Frederic Fages,[m] Anthony D'Aléo,[flm]* Fabrice Mathevet[ac]* and Chihaya Adachi [abn]*

We report on an improved melt-processing method to prepare organic semiconducting layers with large crystal size and enhanced charge carrier mobilities. The organic compound used in this work is a solution-processable oligo(*p*-phenylene vinylene) derivative substituted at both ends with pyrene moieties. Accurate control of the temperature during the recrystallization of this compound from the melt enables the formation of large single crystal monodomains in thin films. The melt-processed organic layer shows in transistor configuration higher mobilities than in spin-coated films, which can be attributed to the presence of large-size crystalline monodomains as evidenced by X-ray diffraction measurements. We also investigated the photophysical properties of this material in spin-coated and melted films and found an increase of the photoluminescence quantum yield with the size of the crystals in the organic layer. The advantage of this method over the spin coating also allowed to observe amplified spontaneous emission that was only achieved in the melted film due to its improved luminescence efficiency. Overall, this study demonstrates a simple and versatile method, which does not require the use of any solvent and vacuum, to fabricate organic layers with large crystal size, suitable for the realization of organic electronic and light-emitting devices.

1. Introduction

Organic semiconducting thin films have been widely investigated in the last decades and used in a range of organic electronic devices including organic light-emitting diodes (OLEDs), organic lasers and organic field-effect transistors (OFETs).[1-8] Two kinds of methods based on solution-processing and vacuum vapor deposition are generally used for the fabrication of these organic layers. Solution-processing techniques such as spin-coating, dip-coating and ink-jet printing are very promising for the industrial production of large area organic electronic devices but require large amount of organic solvents.[9-13] In parallel, vacuum vapor deposition has been extensively used for the realization of high performance organic electronic devices but is not necessarily well-adapted for large scale production due to its cost and the waste of organic compounds during the evaporation process. To sort out these issues, several methods to fabricate organic thin films under solvent-free and vacuum free conditions have been proposed including the friction-transfer method,[14] organic vapor jet printing,[15] laser printing,[16] solid-state compression molding[17] and more recently cold and hot isostatic pressure techniques.[18] Another interesting approach based on a template-assisted self-assembly process has been developed to prepare organic liquid crystalline thin films in OFET devices.[19] In this method, powder of the liquid crystal material is melted above its isotropic phase

---

[a] *Center for Organic Photonics and Electronics Research (OPERA), Kyushu University, 744 Motooka, Nishi, Fukuoka 819-0395, Japan. *E-mail: ribierre@opera.kyushu-u.ac.jp, fabrice.mathevet@upmc.fr, adachi@opera.kyushu-u.ac.jp*
[b] *Japan Science and Technology Agency (JST), ERATO, Adachi Molecular Exciton Engineering Project, c/o Center for Organic Photonics and Electronics Research (OPERA), Kyushu University, 744 Motooka, Nishi, Fukuoka 819-0395,*
[c] *Sorbonne Universités, Faculté des Sciences, CNRS, Institut Parisien de Chimie Moléculaire (IPCM), UMR 8232, Chimie des Polymères, 4 Place Jussieu, 75005 Paris, France*
[d] *Sorbonne Universités, Faculté des Sciences, CNRS, Institut des NanoSciences de Paris (INSP), 4 Place Jussieu, 75252 Paris Cedex 05, France*
[e] *Institut de Physique et Chimie des Matériaux de Strasbourg (IPCMS), UMR 7504, CNRS-Université de Strasbourg, 23 Rue du Loess, 67034 Strasbourg Cedex 2, France*
[f] *Department of Physics, Ewha Womans University, Seoul 03760, South Korea. *E-mail: daleo@cinam.univ-mrs.fr*
[g] *Univ. Grenoble Alpes, DCM UMR 5250, F-38000 Grenoble, France*
[h] *Univ. Paris Diderot, Sorbonne Paris Cité, ITODYS, UMR 7086 CNRS, 15 rue Jean-Antoine de Baïf, 75205 Paris Cedex 13, France*
[i] *Center for Emergent Matter Science (CEMS), RIKEN, 2-1 Hirosawa, Wako, Japan*
[j] *Elements Chemistry Laboratory, RIKEN Cluster for Pioneering Research (CPR), 2-1 Hirosawa, Wako, Japan*
[k] *Graduate School of Pharmaceutical Sciences, The University of Tokyo, 7-3-1 Hongo, Bunkyo-ku, Tokyo 113-0033, Japan*
[l] *Building Blocks for Future Electronics Laboratory (2-B FUEL), The joint CNRS-Ewha-Yonsei Laboratory, UMI 2002, Seoul, Republic of Korea*
[m] *Aix Marseille Univ, CNRS, CINaM UMR 7325, Campus de Luminy, Case 913, 13288 Marseille, France*
[n] *International Institute for Carbon Neutral Energy Research (WPI-I2CNER), Kyushu University 744 Motooka, Nishi-ku, Fukuoka 819-0395, Japan*

Electronic Supplementary Information (ESI) available: [crystal structure of bis-styryl-pyren, AFM images, SWAXS data in powder, cyclic voltammetry data and OFET data]. See DOI: 10.1039/x0xx00000x temperature, fills by capillarity the active area of the organic electronic devices, and the sample is finally cooled down at room temperature, leading to the formation of a homogeneous and high optical quality organic liquid crystalline layer with homeotropic alignment and good charge carrier mobilities. Surprisingly this method has not been employed so far to fabricate high mobility organic field-effect transistors based on highly crystalline organic semiconductors able to form organic single crystals via conventional techniques such as physical vapor deposition or solution-processing. However, this melt-processing route has also been used to form highly crystalline organic layers in light-emitting organic microcavities showing polariton lasing under optical pumping.[20] While this approach is potentially very interesting to get crystalline organic light-emitting structures in a Fabry-Perot microcavity, the small dimension of the single crystal monodomains obtained up to now via this technique has been presumably detrimental to achieve high charge carrier mobilities in OFET device configuration.

In this manuscript, we report on an improved melt-processing method to produce organic semiconductor layers with millimetric single crystal monodomains and enhanced charge carrier mobilities. As shown in Figure 1a, 1,4-di-n-octyloxy-2,5-bis(pyren-1-ylethenyl)benzene (bis-styryl-pyren) is the organic semiconductor used in this study and is a solution-processable oligo(*p*-phenylene vinylene) derivative substituted at both ends with a pyrene moiety.[21] The results demonstrate that the fine control of the temperature during the melt-processing method is the key parameter to prepare high quality organic thin films with large crystal size suitable for the realization of high performance organic field-effect transistors. In addition, the photophysical and amplified spontaneous emission (ASE) properties of Bis-styryl-pyren were investigated in spin-coated and melted films. For this specific organic semiconductor, the results show a clear improvement of the light-emitting properties with the extent of crystallinity of the organic layer. Overall, the proposed improvement of the solvent-free vacuum-free melt-processing route can be applied to a large variety of conjugated molecules and is highly relevant to the field of organic electronics.

2. Experimental

The bis-styryl-pyren molecule was synthesized following a method already published in the literature.[21] Bottom gate organic field-effect transistor (OFET) devices were fabricated onto silicon wafer substrates with a thermally-grown 300 nm thick SiO_2 layer. Interdigitated source/drain (s/d) electrodes were deposited on top of the substrates and were achieved by the sequential thermal evaporation of a 5 nm thick adhesion layer of Cr and a 50 nm thick Au layer. The channel width and length of these bottom contact devices were 76000 μm and 25 μm, respectively. The organic thin films were then deposited by spin-coating at a spin rate of 2000 rpm for 30 s from a 5 mg/ml tetrahydrofuran (THF) solution. Annealing of the spin-coated devices was then carried out on a hot plate in inert atmosphere. To fabricate the melt-processed devices, a glass substrate treated with a self-assembled monolayer of octadecyltrichlorosilane (OTS) was placed on top of a silicon wafer substrate. A very small amount of organic crystalline powder was then placed at one edge of the empty space separating the two substrates and the sample was heated above the melting temperature of the compound in a Linkam THMS 350 heating plate under a nitrogen flow. Then, the organic semiconductor in the isotropic liquid phase filled the empty space by capillary action to form a thin liquid film between the two substrates. After a rapid cooling to crystallize the thin film, the sample was heated again under a polarized optical microscope (Leica) around the melting temperature until the melting of almost all the polycrystalline film took place. When only few single crystal germs were maintained, the sample was cooled down again at a very slow cooling rate (< 0.1 °C min^{-1}) to induce the growth of large millimetric-scale single crystalline monodomains from single crystal germs until room temperature was reached. After removing the top glass substrate, an array of gold s/d electrodes was deposited by thermal evaporation through a shadow mask. Note that the location of the shadow mask was carefully chosen under polarized optical microscope in order to find the best active areas with the largest single crystalline monodomains. In case of the melt-processed devices, a bottom gate top contact configuration was also used for the devices. Channel width and length were in this case equal to 150 and 50 μm, respectively. For the OFET characterization, a semiconductor analyzer (Agilent Technologies, B1500A) and a probe station were used to measure the electrical characteristics of the devices in nitrogen atmosphere.

Electrochemical measurements have been carried out under an argon atmosphere at room temperature in a glove box using a standard one-compartment, three-electrode electrochemical cell using a Bio-logic SP300 potentiostat. Electrochemical investigations have been performed in millimolar freshly distilled THF containing tetra-n-butylammonium hexafluorophosphate $TBAPF_6$ (0.1 M) as the supporting electrolyte. An automatic ohmic drop compensation procedure was systematically implemented prior to recording CV data. CH-instruments vitreous carbon (Ø =3 mm) working electrodes were polished with 1 μm diamond paste (Mecaprex Presi) before each recording. A platinum wire has been used as the counter electrode. Potentials were referenced to an $Ag/AgNO_3$ (10^{-2} M) reference electrode in MeCN+0.1m $TBAPF_6$. Potentials referred to that system can be converted to the ferrocene/ferriciniumcouple by subtracting 87 mV, to the SCE by adding 298 mV or to the NHE reference electrode by adding 548 mV.

The photoluminescence (PL) properties of bis-styryl-pyren were investigated in as-prepared, annealed (at 100 °C for 1 hour) and melted films. The steady-state spectra were measured using a spectrofluorometer (Fluoromax-4, Horiba Jobin Yvon) with an excitation wavelength of 400 nm. PL quantum yield (PLQY) values were determined using an absolute PLQY spectrometer (C11347 Quantaurus-QY, Hamamatsu, Japan). The transient PL characteristics of the films were recorded at room temperature using a Quantaurus-Tau fluorescence lifetime measurement system (C11367-03, Hamamatsu Photonics Co., Japan). The emission wavelength dependence of the PL dynamics was examined using a streak camera (C4334, Hamamatsu Photonics, Japan) and a nitrogen laser operating at a wavelength of 337 nm (Ken-X, Usho Optical Systems, Japan). For the characterization of the ASE properties, the films were photo-excited by a pulsed nitrogen laser at 337 nm with a pulse duration of 800 ps and a repetition rate of 10 Hz. The excitation light was focused onto the samples into a stripe of dimension 0.5 cm x 0.08 cm. The input intensity was varied using a set of neutral density filters. The emission spectra and the output intensity were measured from the edge of the organic layers using an optical fiber coupled to a charge coupled device spectrometer.

Regarding the characterization of the structural properties, the XRD patterns in powder state were obtained with an experimental set-up composed with a linear monochromatic Cu-Kα1 beam (λ = 1.5405 Å) obtained using a sealed-tube generator (900 W) equipped with a bent quartz monochromator. The setup is based on the Guinier transmission geometry and the crude powder was filled in Lindemann capillaries of 1 mm diameter. Diffraction patterns were recorded with a curved Inel CPS 120 counter gas-filled detector linked to a data acquisition computer, and the sample temperature controlled to within ±0.05 °C from the ambient up to 200 °C. The characterization of the structural properties of the spin-coated and melt-processed thin films was performed by 2D grazing incidence X-ray diffraction experiments at PLS-II 9A U-SWAXS beamline of Pohang Accelerator Laboratory in Korea. The thin films were studied on silicon substrates and the X-rays coming from the in-vacuum Undulator (IVU) were monochromated using Si(111) double crystals and focused on a detector consisting of a 2D CCD detector (Rayonix SX165). The distance between sample and detector was around 225 mm and the beam energy was about 11.06 keV (1.121 Å). The thermal phase transitions of bis-styryl-pyren were analyzed by differential scanning calorimetry (DSC) using TA instruments Q2000 under a nitrogen flow. Atomic force microscopy (AFM) experiments were performed in tapping mode, using an apparatus Bruker 3100 and silicon tips, with a resonance around 500 kHz, allowing to specifically probe soft matter.

3. Results and discussion

3.1 Thermal properties of bis-styryl-pyren

The thermal behavior of bis-styryl-pyren was investigated by differential scanning calorimetry (DSC) at a rate of 2 °C min^{-1} on heating and cooling and the thermogram is displayed in Figure 1b. The DSC trace upon heating shows a small endothermic peak at around 84.6 °C (ΔH ≈ 2.4 J g^{-1}), which is attributed to a crystal-to-crystal phase transition related to a slight reorganization of the lattice (vide infra), and a sharp endothermic peak at around 151.6 °C (ΔH ≈ 47 J g^{-1}), which corresponds to the melting to isotropic liquid phase transition. On cooling, these thermal transitions are reversible with the crystallization observed at 119.7 °C and the crystal-to-crystal transition occurring at 85.8 °C. The transition temperatures, phase sequence, and transition enthalpies of bis-styryl-pyren are listed in Table 1.

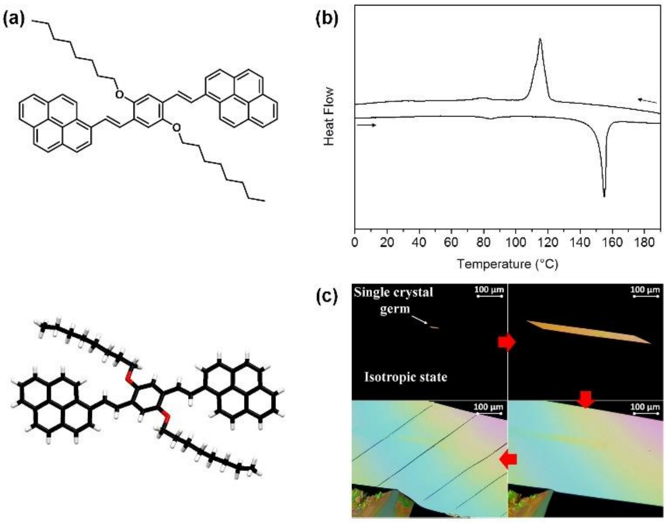

Fig. 1 (a) Chemical structure of bis-styryl-pyren and capped-stick representation extracted from crystallographic data (see Supporting Information). (b) DSC traces recorded at rates of 2°C/min. (c) POM images showing the growth of a large single crystal monodomain from a single crystal germ during the melt-processing.

Table 1. Phase Transition Temperatures and Enthalpy of the bis-styryl-pyren.

compound	transition[a]	T^b (°C)	ΔH (J g^{-1})	transition[a]	T^b (°C)	ΔH (J g^{-1})
Bis-styryl-pyren	Cr→Cr’	84.6[c]	2.4	Cr’→Iso	151.6[c]	47
	Iso→Cr’	119.7[d]	54.7	Cr’→Cr	85.8[d]	2.6

[a] Cr = Crystalline phase 1, Cr’ = Crystalline phase 2, Iso = Isotropic phase. [b] Indicated temperatures are the onsets of the peaks on heating and on cooling. [c] Temperature transition determined during 2nd heating (rate 2°C/min). [d] Temperature transition determined during 2nd cooling (rate 2°C/min).

3.2 Preparation of organic crystalline layer by the melt-processing method

Processing of the crystalline thin layer was carried out in several steps. Firstly, a small amount of bis-styryl-pyren was heated up at 155 °C, in the isotropic liquid phase, to fill out, by capillary action,[22-24] the empty space separating a cover glass and a silicon (or fused silica) wafer. The cover glass, placed on top, was previously treated with a self-assembled monolayer of OTS, in order to reduce its adherence with the final organic film. Second step consists in a rapid cooling down to room temperature, in order to obtain a fine polycrystalline texture. Third, the film was heated again carefully around melting temperature (T = 151.6 °C) and a polarized optical microscope (POM) was used to monitor the process. When almost the entire film had been molten, except a few isolated crystals surrounded by the isotropic liquid (Figure 1c), the sample was cooled down again upon very slow rate (< 0.1 °C min^{-1}). The small residual crystals acted then as crystallization germs and grew to millimetric single monodomains (see Figure 1c and the movie in Supporting Information). In the last step, the weakly adhering OTS-treated cover glass was removed, leaving high quality crystalline organic thin film of 100 to 150 nm thickness (Figure S1). This method therefore proved to be very efficient to process thin films with large single-crystalline domains on top of silicon or fused silica substrates. As shown in Figures 1c and S1, one apparent drawback of this technique could be the formation of cracks during the device cooling to room temperature. This effect is due to the different thermal expansion coefficient between the organic film and the inorganic substrates and could presumably be reduced using appropriate substrate materials such as polydimethylsiloxane (PDMS).

3.3 Structural properties and film morphology

Small-angle X-ray scattering (SWAXS) measurements were carried out on bis-styryl-pyren, in powder state and as a function of temperature. The crystal structure in the powder state is completely different from the arrangement of the single crystals obtained by slow solvent evaporation (Figure S2). Contrarily to the latter, the pristine powder presents a lamellar organization of periodicity 22.8 Å, which is maintained after thermal treatments (Figure S3). The crystal-to-crystal phase transition corresponds to slight change of the molecular packing revealed by small shifts of some wide-angle reflections, which is completely reversible on cooling, consistently with DSC measurements (Figure S4). The powder crystallized from the molten state presents a similar lamellar structure indicating a similar molecular organization (Figure S3).

Likewise grazing incidence X-ray scattering measurements were carried out at room temperature, on bis-styryl-pyren films, namely as-prepared, annealed at 100°C, and melt-processed. The grazing incidence X-ray scattering (GIXS) patterns of the two former, spin-coated, films and of the melt-processed film exhibit a lamellar structure of same periodicity (about 22.3 Å), similar to powder samples (Figure 2). In the three cases, the lamellae are oriented parallel to the substrates as shown by the concentration of the lamellar reflections on the meridian. The three films only differ significantly by the size of the crystallites. For the spin-coated films, the crystallites are mesoscopic and give substantially broadened reflections spots (Figure 2a and 2b). The spot width allows in turn the determination of the average crystallize size from the Scherrer equation, which was found to be 10-15 nm and 15-20 nm, for as prepared and annealed films, respectively, (with shape factor K = 0.9).[25] For the melt-processed films, crystallites are larger than 200 nm, due to the absence of measurable spot broadening. The speckled pattern shape, with discontinuous spots/rings and saturated dots, even suggests very large micrometer-sized crystals, which is indeed in accordance with the optical microscopy observations. As a matter of fact, the population of crystallites in conditions of reflection drastically decreases when the size increases and some domain orientations become then missing while some others get over-represented, resulting in such a characteristic speckled pattern. This is consistent with POM observations made during the melt-processing procedure.

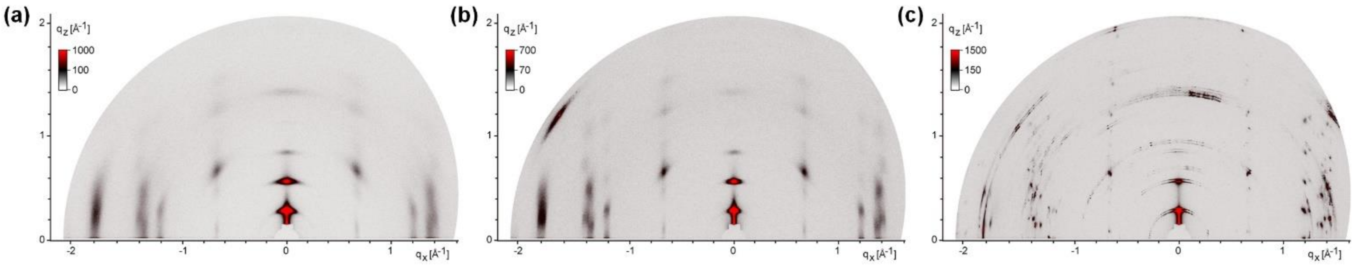

Fig. 2 Grazing incidence X-ray scattering patterns of bis-styryl-pyren in (a) as-prepared and (b) annealed at 100 °C spin coated films, and (c) melt-processed thin film.

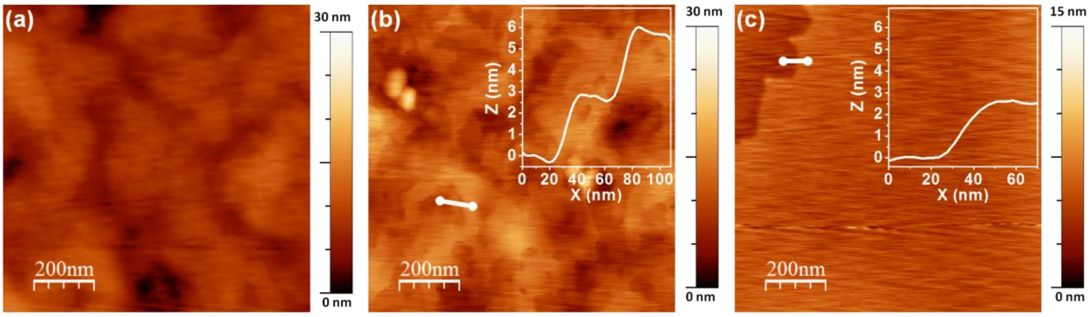

Fig. 3 Topography AFM images of bis-styryl-pyren thin films prepared (a) by spin-coating (as prepared), (b) by spin-coating after annealing at 100°C for 1h, and (c) by melt-processing method. The white insets in (b) and (c) show the terrace step profiles on the surface of thin films along the white lines.

The morphology of spin-coated (as-prepared and annealed) and melt-processed thin films of bis-styryl-pyren was also studied using tapping mode atomic force microscopy (AFM). The AFM topography images are shown in Figure 3. The as-prepared spin-coated thin film (Figure 3a) shows a high number of small-sized crystallites along with a large density of grain boundaries. These crystallites have grown to larger crystals in the spin-coated film after annealing at 100 °C, as revealed by GIXS observations. Indeed, grain sizes reach tens of nanometers within a terrace-and-step morphology. The average value (or multiples) of 2.4 nm being determined for the step height is further consistent with the thickness of one or multiple molecular layers, and with the d-spacings obtained from GIXS (Figure 3b). The melt-processed thin film (Figure 3c) shows very flat, smooth and large domains (above micrometric scale), and molecular steps of around 2.4 nm observable at the large scale of AFM images. Overall, these results demonstrate that the improved melt-processing method yields thin films with very large single-crystalline monodomains and a similar orientation of molecular packing (lamellae oriented parallel to the substrate).

3.4 Charge transport properties of the bis-styryl-pyren thin films

The charge transport properties of the spin-coated and melt-processed organic layers were investigated using a field-effect transistor configuration. Cyclic voltammetry measurements indicated that the highest occupied molecular orbital (HOMO) and the lowest unoccupied molecular orbital (LUMO) energy levels of bis-styryl-pyren are around 5.21 and 2.64 eV, respectively (see Figure S5).[26] Due to its work function matching well with the HOMO energy level of bis-styryl-pyren, gold was chosen for the s/d electrodes in order to investigate the hole transport properties of the organic thin films. Figure 4 shows typical transfer and output characteristics measured in the devices based on spin-coated films before and after a thermal annealing at 100 °C. The square roots of the source/drain current versus gate voltage are also displayed in Figure S6. The results indicate that the spin-coated films operate as p-type semiconductor layers.[27, 28] The output characteristics exhibit clear saturation and linear regimes for negative applied voltages. However, it can be seen from their behavior at low drain-source voltage that contact resistance effects, which seem to be negligible in the as-prepared spin-coated device are slightly increased after the thermal treatment. This effect upon annealing is accompanied by a decrease of the source/drain current. A plausible explanation is that thermal annealing modified not only the crystallite size but also the interface between the metal injecting bottom contact and the active organic layer, causing some changes in the contact resistance of the devices. Hole field-effect mobilities were calculated from the transfer characteristics in the saturation regime, using the standard method.[6]

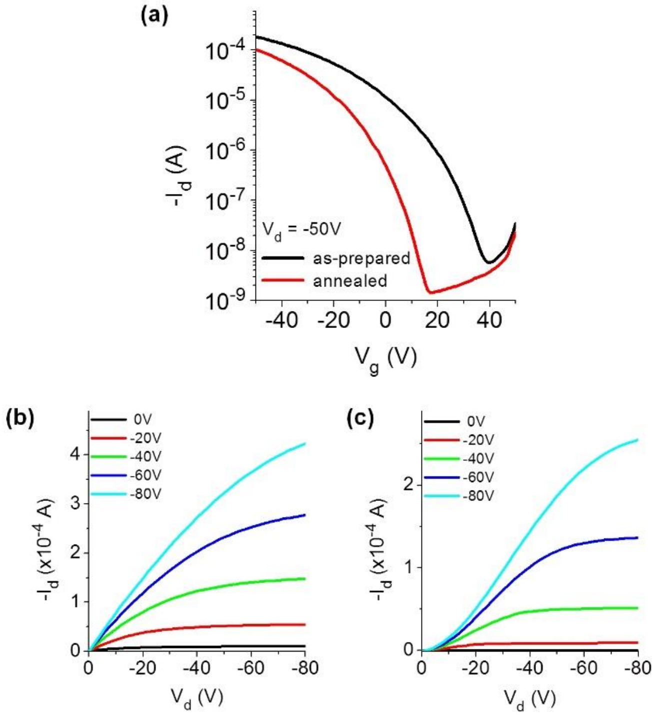

Fig. 4 (a) Transfer characteristics of OFETs based on as-prepared and annealed spin-coated films. (b) and (c) shows the output characteristics of the devices before and after annealing, respectively. Annealing was performed at 100 °C

The average mobility values were determined by testing 10 devices (before and after annealing) prepared from 2 different solutions. The excellent repeatability of the device properties is also illustrated by the histograms in Figure S7. As shown in Table 2, the average hole field-effect mobility of the spin-coated films was found to slightly increase upon annealing at 100 °C from 2.4 x 10^{-3} to 3.5 x 10^{-3} cm²/Vs. The thermal treatment is also found to modify the threshold voltage (V_{th}) from 15 V to -5 V, suggesting an effect of the annealing on the surface states at the interfaces of the organic semiconductor layer. In other words, although the annealed devices show lower source/drain current than the as-prepared devices, we found that the hole mobility of the annealed OFET is higher. This can be understood by looking at the significant changes in V_{th} and in the slopes of the square root of the source/drain current versus gate voltage (see Figure S6). To gain further insights into the role of the annealing on the charge transport of the spin-coated films, we plotted in Figure S8 the hole mobility versus gate voltage. These results are useful to exclude any potential issues in mobility overestimation due to contact problems.[29, 30]

Figure 5 displays the output and transfer characteristics of a representative device based on a melt-processed organic layer. Similarly to the spin-coated polycrystalline thin films, the melt-processed devices exhibit an unipolar p-type conduction with clear linear and saturation regimes in their output characteristics. Noticeably, no significant contact resistance effects can be seen from the behaviour of the output characteristics at low applied voltages. It is worth pointing out that, when using top-contact devices, the area contact is more likely to lead to lower contact resistance than when using line-contact devices. In other words, the use of a top-contact configuration in the melt-processed devices is certainly helpful to minimize contact resistance effects.

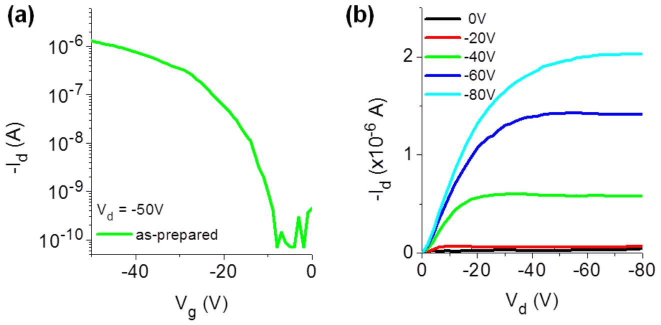

Fig. 5 (a) Transfer and (b) output characteristics of an OFET based on a melt-processed film.

It is important to emphasize here that the device architecture for the spin-coated and melt-processed OFETs is different. The conventional interdigitated bottom s/d electrodes were not used for the melt-processed devices in order to minimize the effects of the cracks on the electrical properties of the film and thus their potential impact on the determination of the field-effect charge carrier mobilities. We should also mention that the position of the shadow mask used for the evaporation of the top s/d electrodes was carefully selected using an optical microscope. This aspect was indeed essential to fabricate melt-processed devices with the cracks in the direction parallel to the transistor channel. Although these values cannot be directly compared with those obtained in the spin-coated devices due to their different architectures, the threshold voltage and the on/off current ratio deduced from the transfer characteristics of the melt-processed devices were typically around – 12 V and over 10^4, respectively. Looking at Figures 4 and 5, it can also be seen that the flowing source-drain current in the device prepared by the melt-processing method is reduced to around 10^{-6} A with respect to about 10^{-4} A when using spin-coated films and interdigitated electrodes. However, taking into account the channel length and width of the device structures and using the standard method to determine the charge carrier mobility in the saturation regime, the hole mobility of the melt-processed device is found to be 5 x 10^{-2} cm^2/Vs, which is more than one order of magnitude higher than the values measured in spin-coated polycrystalline thin films. Although the use of different device architectures certainly affects, to some extent, the determination of the charge carrier mobility, these results are fully consistent with the increase of the crystal size evidenced by the X-ray diffraction results and film morphology shown in Figures 2 and 3, respectively. Previous studies reported on the melt-processing of OFETs based on semiconducting polymers.[31, 32] Although the field-effect mobility of the melted film of bis-styryl-pyren is not increased by several orders of magnitude (in contrast to what we can observe when comparing for instance pentacene single crystal and polycrystalline thin films), the improved melt-processing method described in the present work is found to be suitable for the fabrication of organic electronic devices based on highly crystalline organic materials.

Table 2. Summary of the OFET properties

	Hole mobility (cm^2/Vs)	$I_{on/off}$	V_{th} (V)
As-prepared	2.4 ± 0.4 x 10^{-3}	3 ± 1.2 x 10^4	15± 1
Annealed	3.5 ± 0.4 x 10^{-3}	7.5± 2 x 10^4	-5± 2
Melt-processed	5 ± 1 x 10^{-2}	3± 2 x 10^4	-12± 5

3.5 Photophysical properties of bis-styryl-pyren films

Figure 6a shows the steady-state PL spectra of the as-prepared, annealed and melted bis-styryl-pyren films. The spectrum of the pristine film displays only one main peak with no vibronic progression, which has a maximum emission wavelength at 569 nm. Annealing of the film at 100 °C for one hour leads to a 5 nm blue-shift of the maximum emission wavelength and a substantial broadening of the spectrum. The full-width-at-half-maximum (FWHM) increases indeed from 51 to 94 nm (i.e. 1540 to 2862 cm^{-1}) upon the thermal treatment. It can also be seen that two shoulders appear at about 535 and 595 nm in the spectrum of the annealed sample. In clear contrast with the pristine film, the PL spectrum of the melted sample shows a well-resolved vibronic structure with a maximum emission wavelength at 561 nm. Photoluminescence quantum yield (PLQY) values of 12, 22 and 30 % were obtained in the as-prepared, annealed and melted bis-styryl-pyren film, respectively, indicating a significant improvement of the light-emitting properties with the crystal size in this material. The PL decays measured in the films are shown in Figure 6b. While the PL dynamics in as-prepared and annealed film can be fitted by the sum of two exponential decay functions, the transient curve measured in the melted film follow a single exponential decay with a PL lifetime of 2 ns. It is worth noting that we did not observe any significant emission wavelength dependence of the PL dynamics in the three different films, indicating the presence of only one light-emitting specie in the films. This suggests that changes in molecular configuration are not responsible for the observed variations of PLQY upon thermal treatment. Instead, the GIXS data provided evidence that the crystalline structure of the as-prepared, annealed and melted films was identical and that the morphology of these films only varied by the size of the crystallites. This implies that the observed changes in PLQY cannot be explained by a modification of the molecular arrangement/packing in the film upon thermal treatment.

Exciton diffusion is an important process in organic semiconductors and plays a critical role on the properties of OLEDs and organic solar cells.[33-37] Singlet excitons in these materials can migrate by a Förster-type dipole-dipole coupling and their diffusion length in the films is typically around 5-10 nm.[38-45] Interestingly, a few studies have investigated the influence of the crystalline morphology on the exciton diffusion length in organic thin films.[46, 47] In particular, photophysical measurements in 3,4,9,10-perylenetetracarboxylic dianhydride (PTCDA) polycrystalline thin films showed that singlet exciton diffusion length was strongly enhanced by an increase in the extent of crystalline order.[44] This effect was accompanied by a substantial reduction of the PL quenching at the grain boundaries as the crystallite size in the film was increased. As mentioned above, the GIXS measurements carried out in the present study showed that the crystallite size in the as-prepared and annealed spin-coated bis-styryl-pyren films is around 10-15 and 15-20 nm, respectively. While the exciton diffusion length is several orders of magnitude smaller than the dimensions of the single crystal monodomains in the melt-processed film, its value is in the same order of magnitude as the crystallite sizes in the spin-coated thin films. This implies that a significant number of singlet excitons in the spin-coated films is able to migrate to the grain boundaries where they are more likely to decay non-radiatively. Based on these considerations, we attribute the lower PLQY values and the presence of two time constants in the PL decays of the spin-coated films to a quenching of the singlet excitons at the grain boundaries. Noticeably, the fact that the PL quenching of the spin-coated films is slightly reduced after annealing is consistent with the little increase of the crystallite size upon the thermal treatment. These results provide clear evidence that the melt-processing of highly crystalline organic semiconductor thin films leading to millimetric single crystal monodomains enables to suppress PL quenching at grain boundaries and can thus improve significantly their PL properties.

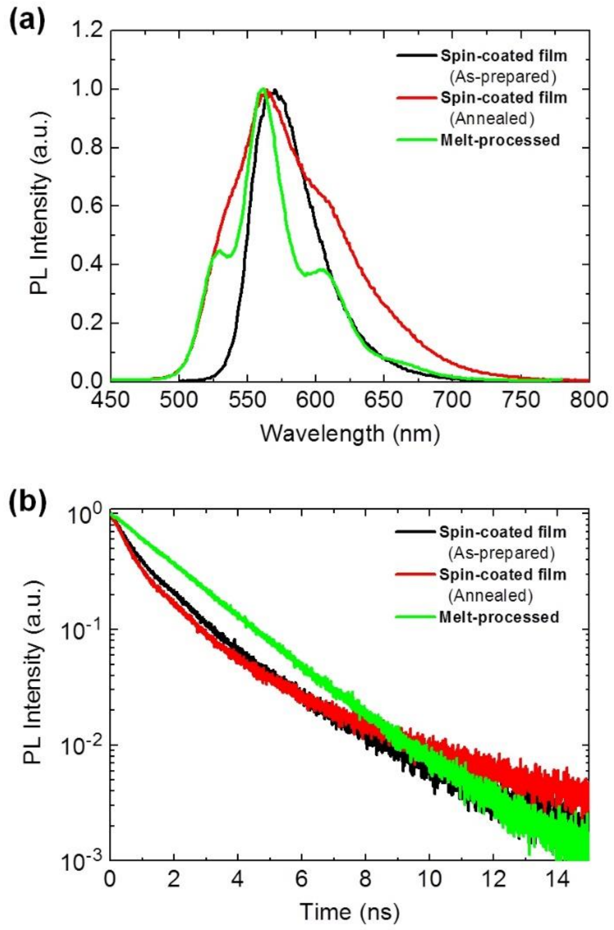

Fig. 6 (a) Steady-state photoluminescence spectra of the pristine, annealed and melted films. Excitation wavelength was 400 nm. (b) Photoluminescence decays measured at room temperature in pristine, annealed and melted films.

Measurements to characterize the amplified spontaneous emission (ASE) properties[48, 49] were carried out in as-prepared, annealed and melted thin films. No ASE could be observed in the as-prepared and annealed spin-coated films using our experimental setup. However, as shown in Figure 7a, a spectral line narrowing due to ASE was clearly observed in the melt-processed thin film as the excitation density was increased from 97.5 to 605 μJ/cm^2. This effect is due to spontaneously emitted photons, which are waveguided in the melt-processed thin film and amplified by stimulated emission. In order to determine the ASE threshold in the melted film, the output intensity and the FWHM of the emission from the edge of the crystalline organic layer were measured as a function of the excitation density. The results are provided in Figure 7b. The ASE threshold is found to be around 200 μJ/cm^2, according to the abrupt changes in the slope efficiency. It can also be seen that the FWHM strongly decreases above the threshold to reach a value of about 4 nm at 900 μJ/cm^2. Noticeably, the ASE threshold measured in the melted bis-styryl-pyren film is much higher than the lowest values reported so far in organic semiconducting thin films.[50-54] However, the most important aspect of this photophysical study is the successful demonstration that the melt-processing method can improve the PL and ASE properties of crystalline organic semiconducting thin films and is suitable for the development of organic light-emitting and organic laser devices. These ASE results also suggest that the waveguiding properties of the organic film have been dramatically improved by the melting process, implying an enhancement of the homogeneity and uniformity of the material. This seems to be consistent with the good repeatability of the OFET data (see the statistics of the OFET parameters in Table 2) obtained with the melt-processed thin films. Since a large spread in optical and electronic device properties[55] is detrimental for applications, this aspect is essential for the potential use of this method in organic optoelectronics.

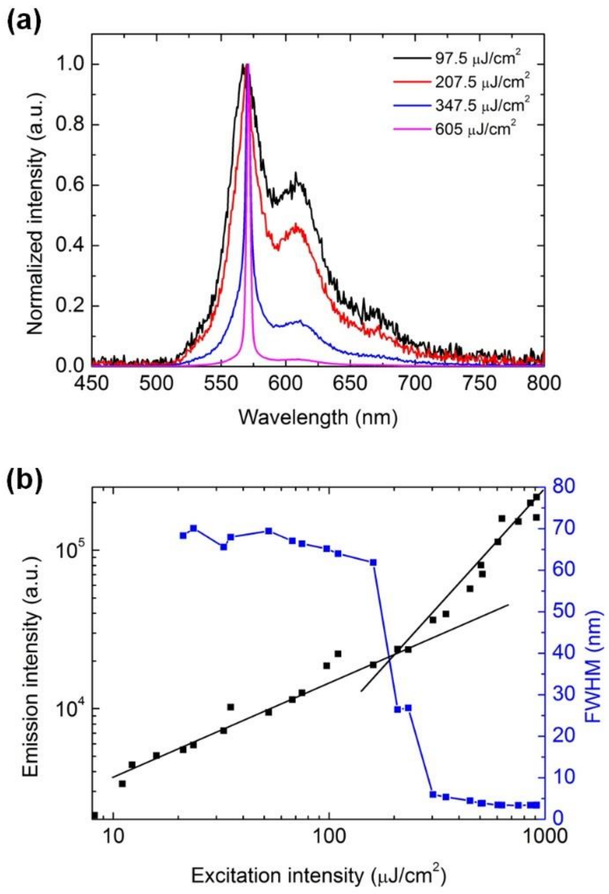

Fig. 7 (a) Emission spectra at different pumping intensities in the melted film below and above the amplified spontaneous emission threshold. (b) Emission output intensity and full-width-at-half-maximum as a function of the pumping intensity.

4. Conclusions

In summary, we propose an improved melt-processing method for the fabrication of organic semiconducting layers with millimetric single crystal monodomains. For this purpose, we used an oligo(*p*-phenylene vinylene) derivative substituted at both ends with a pyrene moiety which is solution-processable and shows a melting temperature around 150 °C. The organic film prepared by melting under solvent-free and vacuum-free conditions presents a morphology with much larger crystal sizes than the spin-coated polycrystalline films. Compared to previous protocols of melt-processing already reported in the literature, this study provides evidence that a fine control and monitoring of the crystal growth under polarized microscope can lead to a significant improvement of the crystalline morphology of the melt-processed organic semiconducting layer. We then demonstrated that the improved melt-processing method can lead to higher charge carrier mobility values. For instance, the hole mobility of bis-styryl-pyren is found to increase indeed from 2.4 x 10^{-3} in the as-prepared spin-coated film to 5 x 10^{-2} cm^2/Vs in the melted sample. This improvement of the charge transport properties upon melting is accompanied by a substantial enhancement of the PLQY. Such a simultaneous optimization of the charge carrier mobility and photophysical properties has been proven to be quite elusive so far in organic semiconductors and can be explained here by the substantial increase of the crystal size and the reduction of the number of grain boundaries in the melt-processed sample. In addition, amplified spontaneous emission could be observed only in the sample prepared by the melt-processing route. Overall, this study demonstrates that the solvent-free vacuum-free melt-processing method can be utilized to fabricate organic electronic and light-emitting devices. This approach is suitable for a large variety of organic semiconductors and, as a consequence, should be of strong interest for future research in the field of organic electronics.

Conflicts of interest

There are no conflicts to declare.

Acknowledgements

This work was supported in part by JST ERATO Grant JPMJER1305, Japan, and by funding of the Ministry of Science, ICT & Future Planning, Korea (2014M3A6B3063706, 2017R1E1A1A01075394). FM acknowledges Kyushu University and the OPERA laboratory for the visiting professor position during this work.

References

1. J. H. Burroughes, D. D. C. Bradley, A. R. Brown, R. N. Marks, K. Mackay, R. H. Friend, P. L. Burns and A. B. Holmes, *Nature*, 1990, **347**, 539.
2. H. Uoyama, K. Goushi, K. Shizu, H. Nomura and C. Adachi, *Nature*, 2012, **492**, 234.
3. D.-H. Kim, A. D'Aléo, X. Chen, A. S. D. Sandanayaka, D. Yao, L. Zhao, T. Komino, E. Zaborova, G. Canard, Y. Tsuchiya, E. Choi, J. W. Wu, F. Fages, J.-L. Brédas, J.-C. Ribierre and C. Adachi, *Nat Photon*, 2018, **12**, 98-104.
4. A. J. C. Kuehne and M. C. Gather, *Chem. Rev.*, 2016, **116**, 12823-12864.
5. A. S. D. Sandanayaka, T. Matsushima, F. Bencheikh, K. Yoshida, M. Inoue, T. Fujihara, K. Goushi, J.-C. Ribierre and C. Adachi, *Sci. Adv.*, 2017, **3**, e1602570.
6. J. Zaumseil and H. Sirringhaus, *Chem. Rev.*, 2007, **107**, 1296-1323.
7. W. Pisula, A. Menon, M. Stepputat, I. Lieberwirth, U. Kolb, A. Tracz, H. Sirringhaus, T. Pakula and K. Müllen, *Adv. Mater.*, 2005, **17**, 684-689.
8. R. H. Kim, H. J. Kim, I. Bae, S. K. Hwang, D. B. Velusamy, S. M. Cho, K. Takaishi, T. Muto, D. Hashizume, M. Uchiyama, P. André, F. Mathevet, B. Heinrich, T.

Aoyama, D.-E. Kim, H. Lee, J.-C. Ribierre and C. Park, *Nat Commun*, 2014, **5**, 3583.

9. Y. Yuan, G. Giri, A. L. Ayzner, A. P. Zoombelt, S. C. B. Mannsfeld, J. Chen, D. Nordlund, M. F. Toney, J. Huang and Z. Bao, *Nature Comm*, 2014, **5**, 3005.
10. D. T. James, J. M. Frost, J. Wade, J. Nelson and J.-S. Kim, *ACS Nano*, 2013, **7**, 7983-7991.
11. H. Minemawari, T. Yamada, H. Matsui, J. y. Tsutsumi, S. Haas, R. Chiba, R. Kumai and T. Hasegawa, *Nature*, 2011, **475**, 364.
12. A. Pierre, M. Sadeghi, M. M. Payne, A. Facchetti, J. E. Anthony and A. C. Arias, *Adv. Mater.*, 2014, **26**, 5722-5727.
13. D. H. Kim, A. S. D. Sandanayaka, L. Zhao, D. Pitrat, J. C. Mulatier, T. Matsushima, C. Andraud, J. C. Ribierre and C. Adachi, *Appl. Phys. Lett.*, 2017, **110**, 023303.
14. S. Nagamatsu, W. Takashima, K. Kaneto, Y. Yoshida, N. Tanigaki and K. Yase, *Appl. Phys. Lett.*, 2004, **84**, 4608-4610.
15. M. Shtein, P. Peumans, J. B. Benziger and S. R. Forrest, *Adv. Mater.*, 2004, **16**, 1615-1620.
16. P. J. Diemer, A. F. Harper, M. R. Niazi, A. J. Petty, J. E. Anthony, A. Amassian and O. D. Jurchescu, *Adv. Mater. Tech.*, 2017, **2**, 1700167.
17. M. A. Baklar, F. Koch, A. Kumar, E. B. Domingo, M. Campoy-Quiles, K. Feldman, L. Yu, P. Wobkenberg, J. Ball, R. M. Wilson, I. McCulloch, T. Kreouzis, M. Heeney, T. Anthopoulos, P. Smith and N. Stingelin, *Adv. Mater.*, 2010, **22**, 3942-3947.
18. T. Matsushima, A. S. D. Sandanayaka, Y. Esaki and C. Adachi, *Sci. Rep.*, 2015, **5**, 14547.
19. A. Kim, K.-S. Jang, J. Kim, J. C. Won, M. H. Yi, H. Kim, D. K. Yoon, T. J. Shin, M.-H. Lee, J.-W. Ka and Y. H. Kim, *Adv. Mater.*, 2013, **25**, 6219-6225.
20. S. Kéna-Cohen and S. R. Forrest, *Nat Photon*, 2010, **4**, 371.
21. T. Lelaidier, T. Leoni, A. Ranguis, A. D'Aléo, F. Fages and C. Becker, *J. Phys. Chem. C*, 2017, **121**, 7214-7220.
22. J.-C. Ribierre, L. Zhao, M. Inoue, P.-O. Schwartz, J.-H. Kim, K. Yoshida, A. S. D. Sandanayaka, H. Nakanotani, L. Mager, S. Méry and C. Adachi, *Chem. Commun.*, 2016, **52**, 3103-3106.
23. J.-H. Kim, M. Inoue, L. Zhao, T. Komino, S. Seo, J.-C. Ribierre and C. Adachi, *Appl. Phys. Lett.*, 2015, **106**, 053302.
24. J. C. Ribierre, T. Aoyama, T. Kobayashi, T. Sassa, T. Muto and T. Wada, *J. Appl. Phys.*, 2007, **102**, 033106.
25. D.-M. Smilgies, *J. Appl. Cryst.*, 2013, **46**, 286.
26. J. Li, M. Wang, S. Ren, X. Gao, W. Hong, H. Li and D. Zhu, *J. Mater. Chem.*, 2012, **22**, 10496-10500.
27. J. Deng, Y. Xu, L. Liu, C. Feng, J. Tang, Y. Gao, Y. Wang, B. Yang, P. Lu, W. Yang and Y. Ma, *Chem. Commun.*, 2016, **52**, 2370-2373.
28. J. Deng, J. Tang, Y. Xu, L. Liu, Y. Wang, Z. Xie and Y. Ma, *Phys Chem Chem Phys*, 2015, **17**, 3421-3425.
29. Y. Zhao, X. Zhao, M. Roders, A. Gumyusenge, A. L. Ayzner and J. Mei, *Adv. Mater.*, 2016, **29**, 1605056.
30. L. Qiu, Q. Xu, M. Chen, X. Wang, X. Wang and G. Zhang, *J. Mater. Chem.*, 2012, **22**, 18887-18892.
31. E. G. Bittle, J. I. Basham, T. N. Jackson, O. D. Jurchescu and D. J. Gundlach, *Nature Comm.*, 2016, **7**, 10908.
32. H. Sirringhaus, *Adv. Mater.*, 2014, **26**, 1319-1335.
33. M. A. Baldo, C. Adachi and S. R. Forrest, *Phys. Rev. B*, 2000, **62**, 10967-10977.
34. E. B. Namdas, A. Ruseckas, I. D. W. Samuel, S.-C. Lo and P. L. Burn, *Appl. Phys. Lett.*, 2005, **86**, 091104.
35. H. Y. Shin, J. H. Woo, M. J. Gwon, M. Barthelemy, M. Vomir, T. Muto, K. Takaishi, M. Uchiyama, D. Hashizume, T. Aoyama, D. W. Kim, S. Yoon, J. Y. Bigot, J. W. Wu and J. C. Ribierre, *Phys. Chem. Chem. Phys.*, 2013, **15**, 2867-2872.
36. G. J. Hedley, A. Ruseckas and I. D. W. Samuel, *Chem. Rev.*, 2017, **117**, 796-837.
37. S. R. Scully and M. D. McGehee, *J. Appl. Phys.*, 2006, **100**, 034907.
38. J. D. A. Lin, O. V. Mikhnenko, J. Chen, Z. Masri, A. Ruseckas, A. Mikhailovsky, R. P. Raab, J. Liu, P. W. M. Blom, M. A. Loi, C. J. García-Cervera, I. D. W. Samuel and T.-Q. Nguyen, *Mater. Horiz.*, 2014, **1**, 280-285.
39. P. E. Shaw, A. Ruseckas and I. D. W. Samuel, *Adv. Mater.*, 2008, **20**, 3516-3520.
40. D. E. Markov, E. Amsterdam, P. W. M. Blom, A. B. Sieval and J. C. Hummelen, *J. Phys. Chem. A*, 2005, **109**, 5266-5274.
41. T. Főrster, *Discuss. Faraday Soc.*, 1959, **27**, 7-17.
42. J. C. Ribierre, A. Ruseckas, I. D. W. Samuel, H. S. Barcena and P. L. Burn, *J. Chem. Phys.*, 2008, **128**, 204703.
43. A. Ruseckas, J. C. Ribierre, P. E. Shaw, S. V. Staton, P. L. Burn and I. D. W. Samuel, *Appl. Phys. Lett.*, 2009, **95**, 183305.
44. M. A. Stevens, C. Silva, D. M. Russell and R. H. Friend, *Phys. Rev. B*, 2001, **63**, 165213.
45. R. R. Lunt, N. C. Giebink, A. A. Belak, J. B. Benziger and S. R. Forrest, *J. Appl. Phys.*, 2009, **105**, 053711.
46. R. R. Lunt, J. B. Benziger and S. R. Forrest, *Adv. Mater.*, 2009, **22**, 1233-1236.
47. T. K. Mullenbach, K. A. McGarry, W. A. Luhman, C. J. Douglas and R. J. Holmes, *Adv. Mater.*, 2013, **25**, 3689-3693.
48. M. D. McGehee, R. Gupta, S. Veenstra, E. K. Miller, M. A. Díaz-García and A. J. Heeger, *Phys. Rev. B*, 1998, **58**, 7035-7039.
49. N. Tessler, N. T. Harrison and R. H. Friend, *Adv. Mater.*, 1999, **10**, 64-68.
50. E. Y. Choi, L. Mazur, L. Mager, M. Gwon, D. Pitrat, J. C. Mulatier, C. Monnereau, A. Fort, A. J. Attias, K. Dorkenoo, J. E. Kwon, Y. Xiao, K. Matczyszyn, M. Samoc, D. W. Kim, A. Nakao, B. Heinrich, D. Hashizume, M. Uchiyama, S. Y. Park, F. Mathevet, T. Aoyama, C. Andraud, J. W. Wu, A. Barsella and J. C. Ribierre, *Phys. Chem. Chem. Phys.*, 2014, **16**, 16941-16956.
51. H. Nakanotani, S. Akiyama, D. Ohnishi, M. Moriwake, M. Yahiro, T. Yoshihara, S. Tobita and C. Adachi, *Adv. Funct. Mater.*, 2007, **17**, 2328-2335.
52. T. Aimono, Y. Kawamura, K. Goushi, H. Yamamoto, H. Sasabe and C. Adachi, *Appl. Phys. Lett.*, 2005, **86**, 071110.
53. J. C. Ribierre, G. Tsiminis, S. Richardson, G. A. Turnbull, I. D. W. Samuel, H. S. Barcena and P. L. Burn, *Appl. Phys. Lett.*, 2007, **91**, 081108.
54. T.-W. Lee, O. O. Park, D. H. Choi, H. N. Cho and Y. C. Kim, *Appl. Phys. Lett.*, 2002, **81**, 424-426.
55. W. Deng, X. Zhang, H. Dong, J. Jie, X. Xu, J. Liu, L. He, L. Xu, W. Hu and X. Zhang, *Mater. Today*, 2018, DOI: https://doi.org/10.1016/j.mattod.2018.07.018,